Journal of Hydrology 615 (2022) 128666

Contents lists available at ScienceDirect

Journal of Hydrology

journal homepage: www.elsevier.com/locate/jhydrol

Research papers

Fully-covered bathymetry of clear tufa lakes using UAV-acquired overlapping images and neural networks

Jinchen He [a,b], Jiayuan Lin [a,b,*], Xiaohan Liao [c]

[a] Chongqing Jinfo Mountain Karst Ecosystem National Observation and Research Station, School of Geographical Sciences, Southwest University, Chongqing 400715, China
[b] Chongqing Engineering Research Center for Remote Sensing Big Data Application, School of Geographical Sciences, Southwest University, Chongqing 400715, China
[c] Institute of Geographic Sciences and Natural Resources Research, Chinese Academy of Sciences, Beijing 100101, China

ARTICLE INFO

Keywords:
Tufa lake
Unmanned aerial vehicle (UAV)
Bathymetry
Optical image
Neural network
Digital bathymetric map (DBM)

ABSTRACT

Accurate and updated bathymetric data is of great significance for the management and protection of alpine tufa lakes. In recent years, unmanned aerial vehicle (UAV)-borne optical remote sensing has become a cost-effective technique for obtaining water depth of small and clear waters like tufa lakes. UAV-based bathymetry can be categorized into photogrammetric approach and spectrally derived approach. Photogrammetric bathymetry is contactless but invalid in water areas with uniform texture, while spectral-based bathymetry requires a large amount of in-situ depth measurements. In this paper, we combined the strengths of the two bathymetric methods to retrieve the depth of clear tufa lakes using neural networks. The surface elevation and orthoimage were first produced from UAV-acquired overlapping images, and then water color-depth tie points were sampled in the orthoimage and refraction-corrected bathymetric map. Next, the shallow and deep neural networks were separately used to train the regression models for predicting water depth. Lastly, the combined bathymetric methods were compared with the single ones in terms of effective spatial coverage and bathymetry accuracy. The results indicated that the combined methods were superior to single bathymetric methods in fully-covered bathymetry of clear tufa lakes. The shallow neural network-based model achieved the highest accuracy, with the coefficient of determination (R^2) of 0.91 and the Root Mean Square Error (RMSE) of 1.12 m, whereas the deep neural network-based model increased the details of water depth distribution.

1. Introduction

Bathymetric survey is of great significance for the management and protection of alpine tufa lakes. As a part of surface karst sedimentary landforms, transparent blue-green tufa lakes have high tourism and scientific value (Currás et al., 2012; Li et al., 2020). However, global climate change, frequent geological disasters and over-exploitation of tourism resources make the tufa lake landscape face the risk of degradation (Liu, 2017; Qiao et al., 2016). Accurate and updated water depth data is very critical for the monitoring and management of these lakes. However, depth measurement using sonar not only consumes huge resources, but also is not suitable for shallow waters (Mandlburger, 2021).

Satellite derived bathymetry (SDB) estimates the depth of shallow waters through remotely sensed satellite data, which has been utilized since the 1970s (Lyzenga, 1978). The technique was initially developed to retrieve water depth based on the spectral information of satellite imagery. In most cases, it follows the physical basis of exponential attenuation of optical signal in the water column. The bathymetric retrieval techniques are generally built upon either physical principles or empirical models (Niroumand-Jadidi et al., 2020). The analysis of radiative transfer process is the basis of physical techniques, while the relationships between spectrally derived features (e.g. band ratios) and water depth should be established for empirical techniques. Therefore, physical bathymetric techniques usually need to conduct accurate atmospheric correction, and empirical techniques require to do numerous in-situ measurements (Zhou et al., 2021). As a result, a large amount of additional workload has to be added in water depth retrieval. Recently, satellite two-media photogrammetry avoided these limitations and provided spatially extensive method for bathymetric mapping (Hodúl et al., 2018). But it cannot satisfy the requirements of high-resolution

* Corresponding author at: Chongqing Jinfo Mountain Karst Ecosystem National Observation and Research Station, School of Geographical Sciences, Southwest University, Chongqing 400715, China.
E-mail address: joeylin@swu.edu.cn (J. Lin).

https://doi.org/10.1016/j.jhydrol.2022.128666
Received 31 March 2022; Received in revised form 4 September 2022; Accepted 10 October 2022
Available online 2 November 2022

and fine-scale bathymetry in alpine tufa lakes.

In recent years, unmanned aerial vehicles (UAVs), especially mini-UAVs and drone technologies, have developed very rapidly, making them a popular remote platforms (Xiang et al., 2019; Chen et al., 2022). When taken as a whole system of components (UAV, sensor, ground station, etc.), their technical terms are also known as unmanned aircraft systems (UAS) or remotely piloted aircraft systems (RPAS) (Colomina and Molina, 2014; Alvarez et al., 2018). At the moment, UAV-based remote sensing has been increasingly used in forest surveys and management (Otero et al., 2018; Lin et al., 2022), geological surveys (Colica et al., 2021), hydrological research (Vélez-Nicolás et al., 2021) and archaeological surveys (Rouse and Krumnow, 2020), etc. Meanwhile, structure-from-motion and multi-view stereo (SfM-MVS) algorithms have become sophisticated, but they still follow the photogrammetric principles (Westoby et al., 2012; Fonstad et al., 2013). Hence, UAV-based SfM-MVS photogrammetry is frequently used for geoscience applications owing to its advantages of low cost and high resolution (Eltner et al., 2016; Meinen and Robinson, 2020; Granados-Bolaños et al., 2021). Previous studies have demonstrated that the UAV-acquired aerial images with high overlap can produce high-resolution and high-accuracy digital elevation models (DEMs) (James and Robson, 2014). Under the conditions of good illumination and transparent water, overlapping UAV imagery can also derive underwater topography (Woodget et al., 2015; Woodget et al., 2019), which is referred to as bathymetry (David et al., 2021; Mandlburger, 2021). Therefore, UAV-based remote sensing has become an effective technique for retrieving depths of small and transparent tufa lakes (He et al., 2021).

Similar to existing satellite bathymetric models, UAV-based bathymetry can be categorized into spectrally derived bathymetry and photogrammetric bathymetry (Dietrich, 2017; Shintani and Fonstad, 2017; Kim et al., 2019). The spectral-based bathymetry was principally derived from the overlapping images taken by UAV-loaded visible/multispectral cameras (Kim et al., 2019; Rossi et al., 2020). The empirical SDB models, such as log-linear inversion model, Stumpf model, and optimal band ratio analysis (OBRA) (Lyzenga, 1978; Stumpf et al., 2003; Legleiter et al., 2009), have been applied to bathymetric survey, achieving a depth accuracy of about 20 cm in shallow waters (Rossi et al., 2020). As for UAV-based photogrammetric bathymetry, the refraction correction is necessary to be conducted in the general UAV-SfM workflow. This kind of approaches is essentially geometrical analysis that aims to eliminate the refraction effect of light at the air–water interface. One simplified post-processing solution is to correct the initial water depth derived from the resulting DEMs using a constant scale factor (Woodget et al., 2015). Some other approaches deal with the refraction effect in the process of bundle adjustment (Maas, 2015; Mulsow et al., 2018), or build a refraction correction model based on SfM-MVS photogrammetric point cloud (Dietrich, 2017).

However, it is very difficult for the photogrammetric bathymetry to identify effective tie points in overlapping images of the water area with uniform texture (Mandlburger, 2019), so the bathymetric map frequently fails to cover the entire tufa lake. In contrast, spectral-based bathymetry usually works better in the low texture areas of a tufa lake, but requires a number of in-situ depth measurements (He et al., 2021). Therefore, the spectral-based and photogrammetric techniques complement each other, and their integration may improve the effective coverage of bathymetry (Slocum et al., 2020). Literature review indicates that the combination of photogrammetric and spectrally derived bathymetry provides an increase of up to 61 % in spatial coverage compared to either of the two approaches (Slocum et al., 2020). The combined approach can be applied to the bathymetry of alpine tufa lakes, and is expected to address the problem of missing image matching points in low texture areas.

As homologous products from UAV-acquired images, the orthoimage and DEM share the same spatial and temporal reference. The digital number (DN) of spectral bands can be obtained from a SfM-MVS derived orthoimage (Starek and Giessel, 2017), while the initial water depth can be extracted from a SfM-MVS derived digital surface model (DSM) (Shintani and Fonstad, 2017; Meinen and Robinson, 2020). Since the UAV-acquired optical images are usually not preprocessed with the radiometric correction, DN values will be used for water depth inversion instead of the reflectance ones (Kim et al., 2019). The photogrammetric bathymetry can provide appropriate reference data for training, validation, and testing of spectral-based bathymetric models like airborne Lidar bathymetry (Mandlburger et al., 2021). Machine learning approaches including neural networks (e.g. back-propagation artificial neural networks) usually do well in establishing the relationship between spectral features and reference data (Danesh-Yazdi et al., 2021; Feng et al., 2021; Guo et al., 2021a; Slocum et al., 2020). Therefore, the combined approaches using neural networks will not only effectively expand the bathymetric coverage, but also make it possible for completely non-contact bathymetry in alpine tufa lakes.

The structure of this paper is composed of the following sections. Section 2 introduces study area and UAV data acquisition, and then describes the methods including UAV data processing, single/combined bathymetric approaches and accuracy assessment. Section 3 presents the water depth maps derived by bathymetric models, their bathymetry accuracies, and improvements from neural network-based methods. The transferability and deficiencies of combined bathymetric models are discussed in Section 4. The conclusions of this study are drawn in Section 5.

2. Materials and methods

2.1. Study area and data

2.1.1. Study area

Jiuzhai Valley is located in the south of Minshan Mountain and the northeast of Gongga Mountain. The terrain in the valley fluctuates, and the main valley has the length of greater than 30 km. In terms of geology and geomorphology, Jiuzhai Valley is located in the transition zone of Qinghai-Tibet Plateau and Sichuan Basin. Hence, the complex geologic history and widely distributed carbonate developed large-scale karst tufa deposits. In terms of climate and hydrology, Jiuzhai Valley is included in the humid plateau climate. There are 114 alpine lakes mostly distributed in groups with various sizes. The water system in Jiuzhai Valley has a “Y” shape, which finally flows into the Jialing River. The waters from Rize Valley and Zechawa Valley in the upstream converge into Shuzheng Valley in the downstream (Fig. 1). The study area is situated in Shuzheng Valley, where many blue-green tufa lakes are distributed, including Shuzheng Lakes, Lying Dragon Lake, Spark Lake and Double-Dragon Lake.

Spark Lake, also known as Huohuahai Lake (Guo et al., 2021b), is a typical tufa lake located between Double-Dragon Lake and Lying Dragon Lake in Shuzheng Valley. It is roughly in a triangular shape with a side length of about 150 m. The flow velocity in the lake was slow, and the lake surface was calm. On August 8, 2017, an earthquake measuring 7.0 on the Richter scale struck Jiuzhaigou County, northern Sichuan Province (Lei et al., 2017). The epicenter was located in Bimang Village, 5 km west of Jiuzhai valley. The earthquake triggered landslides and collapses in various locations in Jiuzhaigou Scenic Area, including Nuorilang Waterfall, Spark Lake and other scenic spots. The tufa barrage at the downstream side of Spark Lake collapsed in the earthquake. As a result, the lake water was almost drained out and the lake basin was exposed. Earthquake caused landslips in some tufa mounds of the lake, and a small amount of flood remained in the downstream lake basin. Subsequently, the collapsed barrage of Spark Lake was rebuilt, but the morphology of original lake bed has not been significantly changed. Therefore, it is an ideal test site for studying on bathymetry of tufa lakes.

2.1.2. UAV-acquired images

The raw aerial images in this study were acquired by two different unmanned aircrafts before and after Jiuzhaigou earthquake. A fixed-

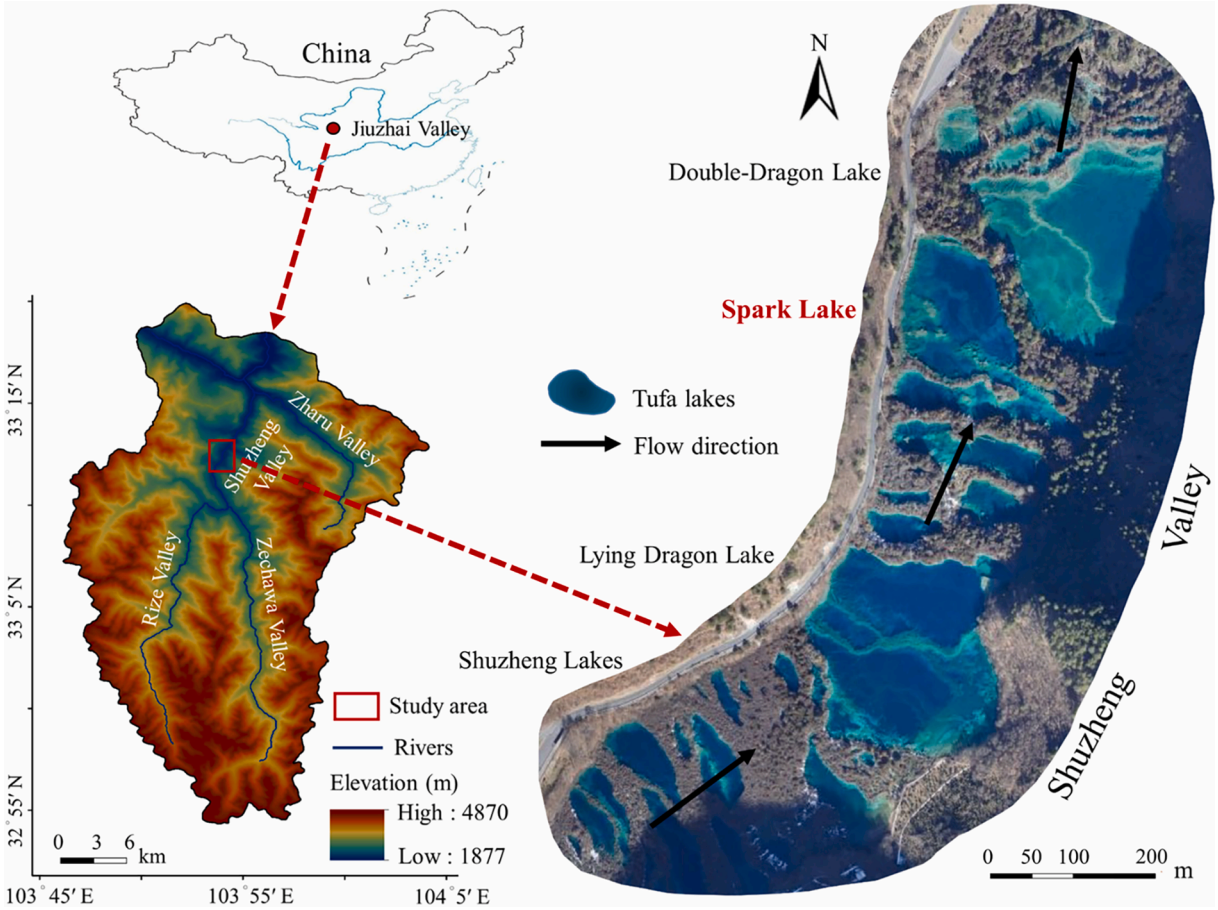

Fig. 1. Location of study area. The major sub valleys of Jiuzhai Valley are marked, and the tufa lakes in study area are tagged.

wing UAV (FEIMA F1000) was used before the earthquake to obtain images covering the whole Shuzheng Valley (December 9, 2016), while a quad-rotor drone (DJI Phantom4 Pro) was focused on the test site, Spark Lake after the earthquake (October 10, 2018). The fixed-wing UAV was equipped with a consumer-grade digital camera (SONY ILCE-5100), and the quad-rotor drone with specially designed camera (DJI FC6310). Both UAVs were loaded with inertial measurement unit (IMU) and global positioning system (GPS) to measure their instantaneous three-dimensional (3D) position and orientation information (i.e. external orientation elements) during airborne surveys. The spatial resolutions of overlapping images collected by the fixed-wing UAV and the multi-rotor drone were 10 cm and 5 cm, respectively.

2.2. *Methods and validation*

The major procedures of retrieving depth of clear tufa lakes include

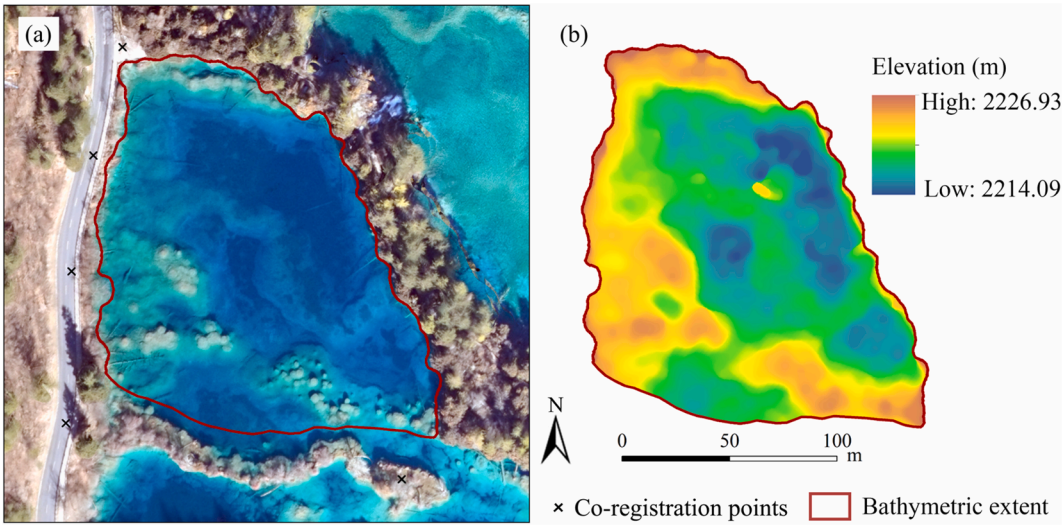

Fig. 2. (a) Orthoimage with co-registration points and bathymetric extent, and (b) surface elevation of Spark Lake.

explanation of UAV data processing, single and combined bathymetric methods, and validation of bathymetric accuracy.

2.2.1. Surface processing and sampling

Aerial triangulation is also called SfM in computer vision (Xiang et al., 2019). The commercial SfM software (i.e. Pix4D 4.4.10) was applied to processing UAV-acquired images through the steps of auto-triangulation, orthorectification and mosaicking. The purpose was to generate orthoimage and surface elevation of the study site (Fig. 2). SfM-MVS, the state-of-art algorithms for 3D surface reconstruction, are not only the core of aerial triangulation processing, but also the key to producing the final products (dense point cloud, orthoimage, DSM, etc.). The SfM-MVS processing starts with the automatic extraction of tie points in the UAV-acquired overlapping images. SfM simultaneously obtains camera poses and parameters via bundle adjustment, and generates sparse point cloud. On the basis of SfM processing, MVS densifies point cloud using multi-view stereo matching algorithms (Smith et al., 2014). Then, the dense point cloud is rasterized to produce the orthoimage and DSM of the study site (Iglhaut et al., 2019).

The spatial co-registration and resampling of pre- and post-earthquake orthoimage and DSM were carried out in GIS software (i.e. ArcGIS 10.3.1). The points used for spatial co-registration were distributed around Spark Lake, and their positions were marked in the pre-earthquake orthoimage as shown in Fig. 2a. In order to keep the size and position of image pixels consistent, the orthoimages and DSMs before and after the earthquake were resampled with ground sample distance (GSD) of 5 cm. The lake surface points were selected along the water's edge from the pre-earthquake orthoimage, and the average value of their elevations was taken as the final water surface elevation (WSE) (Woodget et al., 2019). The calculated WSE was 2,226.93 m, below which the bathymetric extent of the lake basin area was extracted from the pre-earthquake DSM (Fig. 2b). The DSM falling in the bathymetric extent was regarded as the initial DEM, with a minimum elevation of 2,214.09 m. Then, the initial digital bathymetric map (DBM) was obtained through the conversion between the initial DEM and WSE using Eq. (1). Likewise, the post-earthquake "dry depth" of Spark Lake was converted from the DSM of exposed lake bed and the WSE (Fig. 3b).

$$h = WSE - E \quad (1)$$

Where h represents the water depth, WSE is the water surface elevation, and E represents the lake bed elevation.

Based on the pre- and post-earthquake DBMs, the two depth values of each sampling point were collected, while the DN values of red, green and blue bands of sampling points were extracted from the pre-earthquake orthoimage. In the sampling process, we excluded the areas where the surface elevation had been changed or covered by ponding after the earthquake (Fig. 3a). Random sampling was conducted in the selection of sample points, which achieved the relatively balanced distribution of sample points with various water depths. 900 sample points were randomly divided into 600 training points with depth values and DN values, and 300 check points with post-earthquake "dry depth" values. The number distribution of sample points, training points and check points in the various ranges of "dry depths" was shown in Table 1. The training points were only used to establish spectral-based bathymetric models, and the check points were used to validate the accuracies of all bathymetric models including photogrammetric, spectral-based, and neural network-based models.

2.2.2. Single bathymetric methods

Single bathymetric methods can be divided into spectrally derived bathymetry and photogrammetric bathymetry. The pre-earthquake orthoimage and the conversed depth maps before and after the earthquake were taken as the data sources for single bathymetric methods.

Spectrally derived bathymetry in our case was a method to retrieve the water depth by establishing the regression relationship between the band DN values or the combinations in the orthoimage and "dry depth" values after the earthquake. For single band log-linear models, the green band (ln*Green*) was the preferred one for water depth inversion because it showed a stronger capability in penetrating the water body of tufa lakes. For band ratio models, the Stumpf model usually applied the combination of blue band and green band (ln*Blue*/ln*Green*) to retrieve the water depth (Stumpf et al., 2003). In such a model, the longer wavelength (green band) provided the information of water depth change, while the shorter wavelength (blue band) offered the information of bottom type (Legleiter et al., 2009). Compared with band ratio models, the band difference model based on blue band and green band (*Blue-Green*) was more in line with the water color features of transparent tufa lakes (He et al., 2021).

Table 1
Depth distribution of sample points.

Depth range (m)	0–2	2–4	4–6	6–8	8–10	10–12	12–14	Sum
Training points	18	79	112	82	87	143	79	600
Check points	14	36	54	42	34	69	51	300
All points	32	115	166	124	121	212	130	900

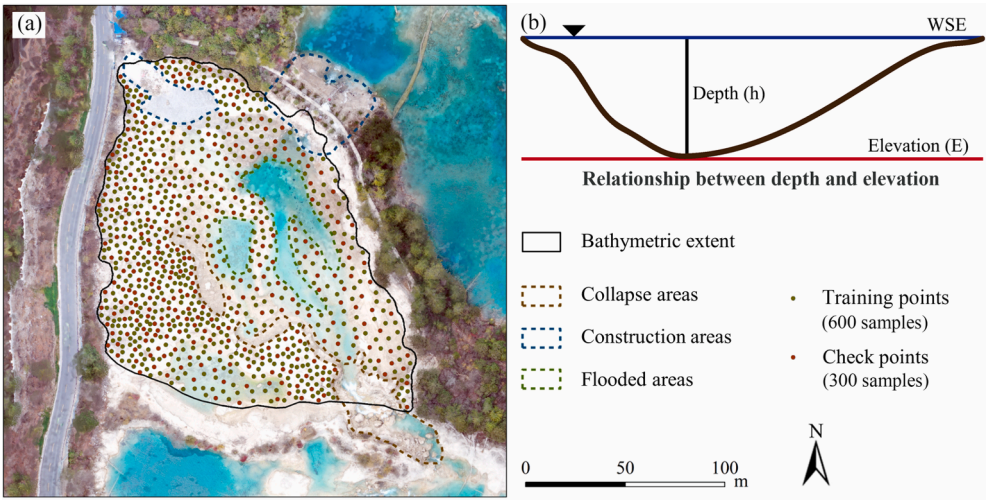

Fig. 3. (a) Distribution of sample points used for bathymetric model training and validation, and (b) the conversion relationship between depth and elevation. WSE is the abbreviation of water surface elevation.

Photogrammetric bathymetry was based on the principle of photogrammetry and supplemented with refraction correction to obtain the actual water depth. The initial DBM directly generated by photogrammetry had a large bias (2 ~ 3 m) and needed to be corrected. The geometry of refraction correction is described by Snell's Law (Eq. (2)). In our study, refraction correction was applied to the initial DBM, and a constant scale factor was used to correct the initial water depth according to the simplified Snell's Law (Alvarez et al., 2018). The refractive index of fresh water (1.34) as the correction factor could generally meet the requirements of water depth estimation (Woodget et al., 2015; Shintani and Fonstad, 2017). In other words, the actual water depth was equal to the initial water depth multiplied by 1.34. The DBM correction could be conveniently realized using the ArcGIS Raster Calculator tool. However, the initial raster DBM derived from dense point cloud would be affected by the quality of point cloud itself. As shown in Fig. 4, the point cloud in low texture areas were missing due to the lack of effective tie points in the dense image matching of aerial auto-triangulation. As a result, photogrammetric bathymetry could not generate bathymetric map effectively covering the entire tufa lake.

$$\frac{\sin(r)}{\sin(i)} = \frac{n_2}{n_1} \tag{2}$$

Where i and r are the incidence angle and refraction angle for light transmitting from air into water. n_1 and n_2 are the refractive indexes of air and water.

2.2.3. Combined bathymetric methods

As the spectral and geometric bathymetric methods complement each other, the combination of them was expected to overcome the shortcomings of single bathymetric methods and establish a fully-covered and non-contact bathymetric method.

Neural network is a machine learning-based operation model, which is composed of a large number of nodes (or neurons) in different layers. Generally, a neural network architecture consists of one input layer, one/multi hidden layer(s), and one output layer (Danesh-Yazdi et al., 2021). Considering the fitting capability of neural networks to non-linear problems, the shallow and deep neural networks were selected to separately fit the training data. The basic way of the combination was to take the refraction-corrected water depth before the earthquake as the depth training data, and establish the relationship between the band DN values in the pre-earthquake orthoimage and water depths using neural network models. The flow chart of combining geometric and spectral methods is shown in Fig. 5.

The preliminary preparation for training the neural network models was to exclude the invalid area in the refraction-corrected DBM, and extract the corrected water color-depth values from the valid area. In our case, the invalid area is the abnormal part of Spark lake with uniform texture (Fig. 4), and it would be excluded during water color-depth tie point sampling. The key to the establishment of bathymetric models was to use neural networks to train the regression models, so as to input spectral features and output the predicted bathymetric values (Guo et al., 2021a). The spectral features here referred to the DN values of red, green and blue bands in the pre-earthquake orthoimage. The neural network models were implemented using the MATLAB (version R2017b) Neural Network toolbox, including a shallow neural network and a deep neural network. The shallow neural network adopted one hidden layer with 5 nodes (N = 5) (Fig. 6a), the deep neural network had three hidden layers (Fig. 6b), and the numbers of hidden layer nodes were 10, 8 and 5, respectively (K = 10, L = 8, and M = 5). The reason for such choices was that complex topologies might lead to over-fitting, while simplistic ones could not accurately predict water depth (Slocum et al., 2020). Furthermore, the shallow neural network was trained with Levenberg-Marquardt back propagation algorithm. The Sigmoid function was used as the activation function of hidden layer neurons (Eqs. (3) and (5)), while the activation function of output layer neurons were linear (Eqs. (4) and (6)) (Danesh-Yazdi et al., 2021). The deep neural network adopted the same activation function of hidden layers, but did more repeated calculations of hidden layers' neurons.

$$g(x) = \frac{1}{1+e^{-x}} \tag{3}$$

$$f(x) = x \tag{4}$$

$$H_q = g\left(\sum_{p=1}^{3} w_{pq}x_p + a_q\right) \tag{5}$$

$$Depth = f\left(\sum_{q=1}^{N} H_q w_q + b\right) \tag{6}$$

Where N is the number of nodes in the hidden layer, w_{pq} is the weight from the input layer to the hidden layer, x_p represents the DN values of

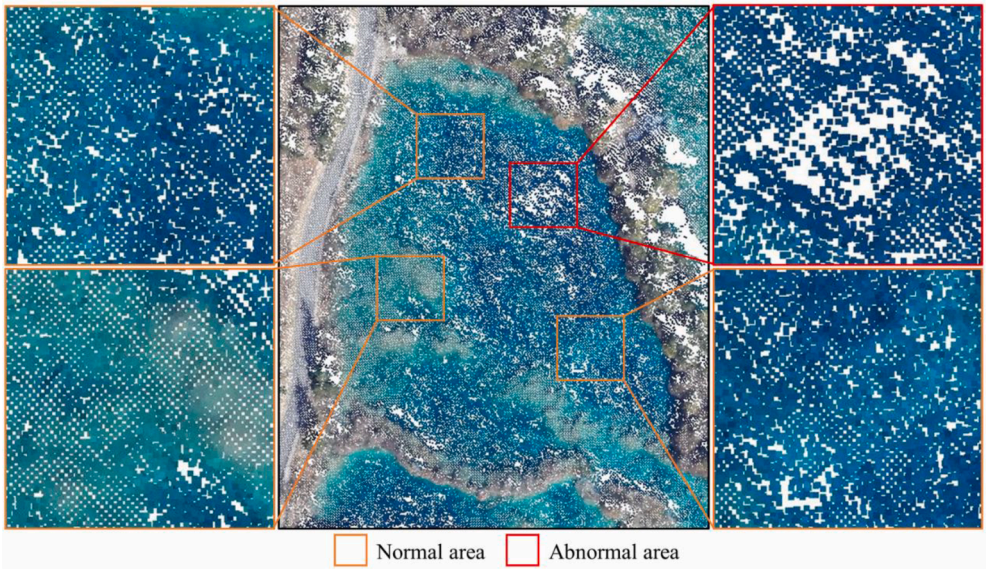

Fig. 4. Dense point cloud of Spark Lake. Normal point clouds are in the orange boxes, while abnormal point cloud is in the red box. (For interpretation of the references to color in this figure legend, the reader is referred to the web version of this article.)

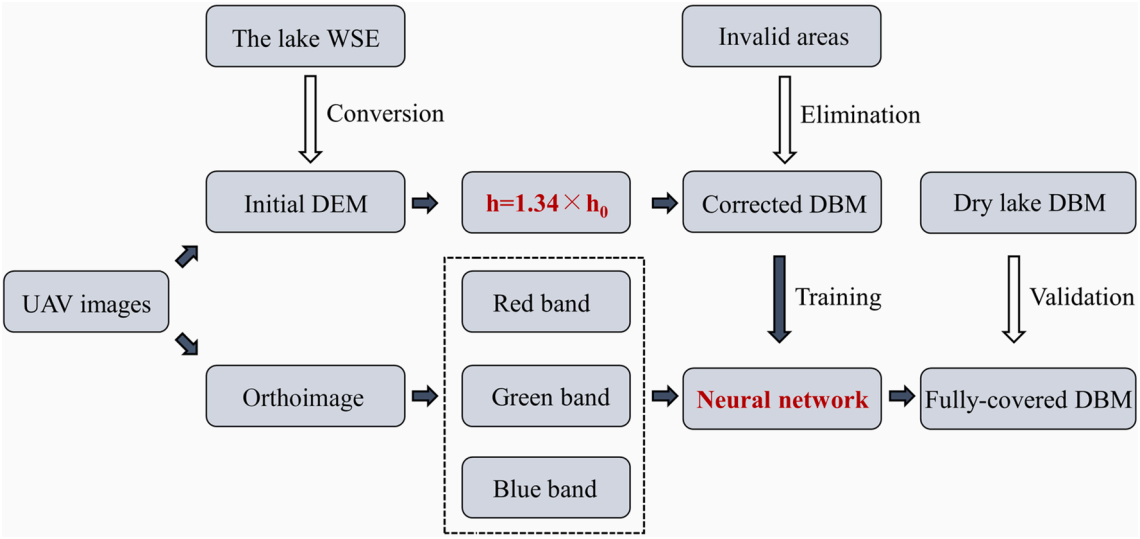

Fig. 5. Flow chart of combining geometric and spectral methods. h is the actual water depth, h_0 is the initial water depth, and DBM is the abbreviation of digital bathymetric map.

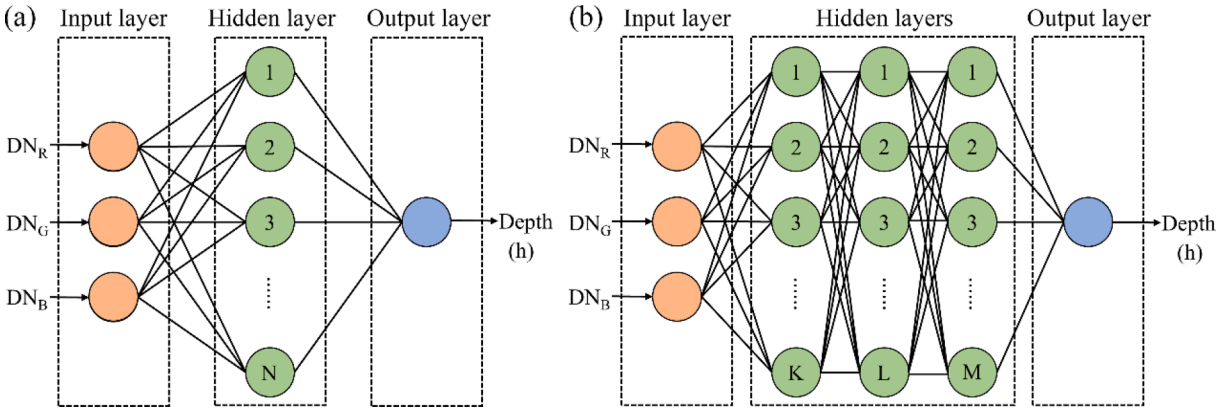

Fig. 6. The architectures of neural network-based bathymetric models. (a) Neural network model with a single hidden layer, and (b) neural network model with multiple hidden layers. DN_R, DN_G and DN_B represent the DN values of red, green and blue bands, respectively. Depth (h) is the water depth value. (For interpretation of the references to color in this figure legend, the reader is referred to the web version of this article.)

red, green and blue bands, a_q is a constant value belonging to the hidden layer's neurons, H_q is the output value of neuron q in the hidden layer, w_q is the weight from the hidden layer to the output layer, b is a constant value relating to the output layer's neuron, and *Depth* represents the predicted water depth.

In addition, the sample data for two neural networks were randomly divided according to the proportion of 7:2:1, namely 70 % was used for training, 20 % for validation, and 10 % for testing. The correlation coefficients (r) in training set, validation set and test set of shallow neural network with single hidden layer and deep neural network with multiple hidden layers were listed in Table 2. The two neural network models were retained after numerous times of training to predict the water depths of the entire bathymetric extent.

2.2.4. Metrics for accuracy assessment

We would use the post-earthquake "dry depths" of the check points as the reference values, and conduct a point-to-point validation to evaluate the performance of various bathymetric models. The statistical validation metrics for accuracy assessment included R^2 (coefficients of determination), RMSE (root mean square error), MAE (mean absolute error) (Eq. (7)) and MRE (mean relative error) (Eq. (8)). The RMSE is non-linear and has a higher weight for larger errors. The MAE is a linear index, and all errors in the samples have the same weight. The MRE is known as percentage error, which is more sensitive to the errors of low value interval.

$$MAE = \frac{1}{n}\sum_{i=1}^{n}|h_i - \widehat{h}_i| \tag{7}$$

$$MRE = \frac{1}{n}\sum_{i=1}^{n}\left|\frac{h_i - \widehat{h}_i}{h_i}\right| \times 100\% \tag{8}$$

Where $\widehat{h}_i$ is the resulting water depth at the location of a check point from various bathymetric models, h_i is the reference water depth, and n is the number of check points.

Table 2
Correlation coefficients (r) of neural network-based bathymetric models.

Neural network model	Training	Validation	Test	All
Shallow neural network	0.9685	0.9523	0.9826	0.9668
Deep neural network	0.9711	0.9797	0.9862	0.9741

3. Results

3.1. DBMs derived by bathymetric models

The six DBMs derived by single and combined bathymetric models were shown in Fig. 7. As a whole, the water depth distributions showed the similar pattern, which was shallow in the west and deep in the east of Spark Lake. In the shallow area, the water depths of all models had little difference except for ln*Green*. But in the deep area, the maximum water depths of models ln*Blue*/ln*Green*, refraction correction and deep neural network exceeded 16 m, while those of models ln*Green*, *Blue-Green* and shallow neural network were less than 16 m.

The DBMs obtained by single bathymetric methods had local anomalies in some areas. For example, there were obvious abnormal depressions scattered near submerged tufa mounds in the dashed rectangles in Fig. 7a, which was retrieved by single band model ln*Green*. As seen in Fig. 7b, the band ratio model ln*Blue*/ln*Green* alleviated the abnormal depressions to a certain extent. The band difference model *Blue-Green* further improved such situation and nearly eliminated the anomalies in those areas (Fig. 7c). In contrast, there were no abnormal depressions near the tufa mounds in the DBM derived by refraction correction model (Fig. 7d). But one abnormal bulge appeared in the dashed circle, where the lake bed had a uniform texture. As for the combined bathymetric methods based on neural network models, there were basically no such anomalies as depressions and bulges in the resulting bathymetric maps (Fig. 7e,f). Compared with single bathymetric methods, the combined ones were effective in the bathymetry of the entire water area of Spark Lake.

3.2. Accuracy assessment of bathymetric models

In order to validate the bathymetric data derived from the six methods, a total of 300 check points in the exposed basin of Spark Lake were collected (Fig. 3). The relationships between the elevation values from the six DBMs and those of the check points were presented as scatter plots in Fig. 8.

As indicated in Fig. 8a, the performance of single band model ln*Green* was the worst among all models, with the R^2 of 0.48 and the RMSE of 2.59 m. The band ratio model ln*Blue*/ln*Green* was slightly better, with the R^2 of 0.74 and the RMSE of 1.82 m, but there was a large deviation in the shallow water (Fig. 8b). Compared with the single band model and the band ratio model, the accuracy of band difference model *Blue-Green* had been significantly improved, with the R^2 of 0.86 and the RMSE of 1.37 m. Moreover, the band difference model nearly performed well in the whole water depth range (Fig. 8c). As the R^2 was 0.88 and the RMSE was 1.32 m (Fig. 8d), refraction correction model achieved the accuracy close to that of the band difference model. The combined bathymetric model based on shallow neural network achieved the highest accuracy, with the R^2 of 0.91 and the RMSE of 1.12 m (Fig. 8e). The RMSE was close to 8 % of the maximum reference depth of Spark Lake. However, the accuracy of the combined model based on deep neural network was not further improved (Fig. 8f). Its R^2 was 0.90 and RMSE was 1.18 m. As indicated in Fig. 8, the derived depths from shallow neural network model and the reference ones from check points had the best consistency among all models, especially in shallow water.

According to statistics in Table 3, the bathymetric model on shallow neural network had the lowest MAE and MRE of 0.89 m and 17.13 %, respectively. Meanwhile, the deep neural network model gained the second place, with the MAE of 0.93 m and the MRE of 19.84 %. Although the band difference model *Blue-Green* and the refraction correction

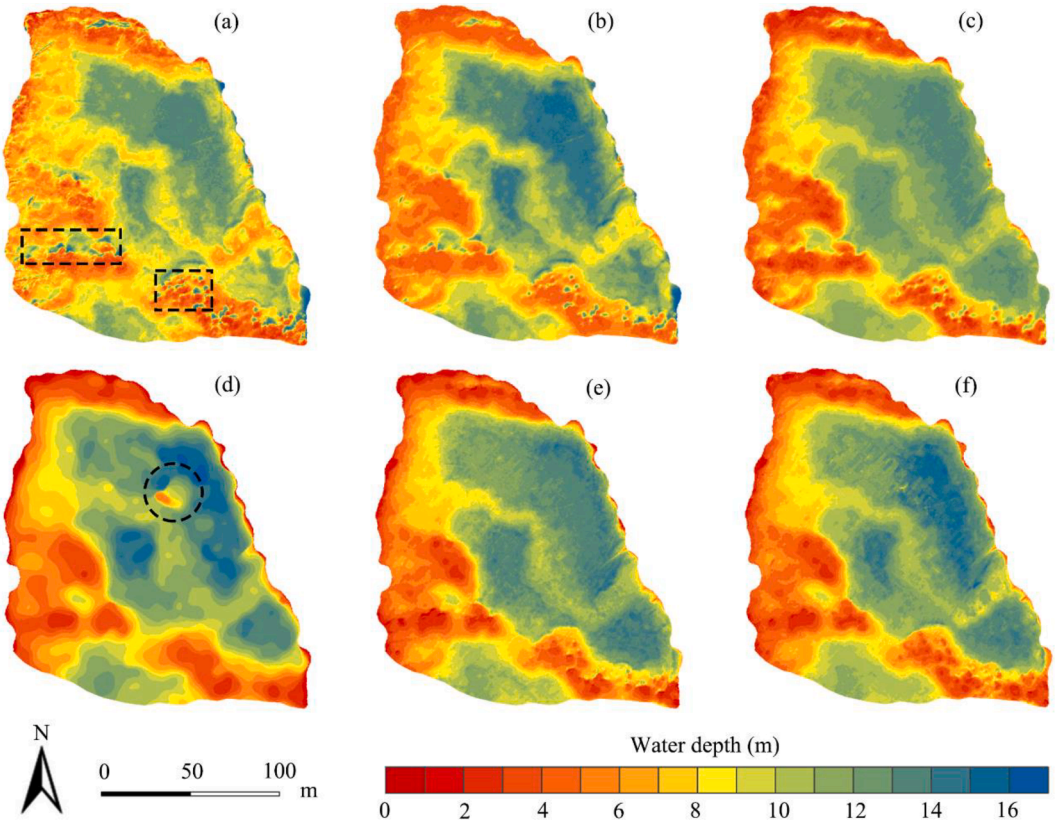

Fig. 7. DBMs of bathymetric models. Water depth inversion models including (a) ln*Green*, (b) ln*Blue*/ln*Green*, and (c) *Blue-Green*; (d) refraction correction model; combined bathymetric models including (e) shallow neural network model, and (f) deep neural network model. (For interpretation of the references to color in this figure legend, the reader is referred to the web version of this article.)

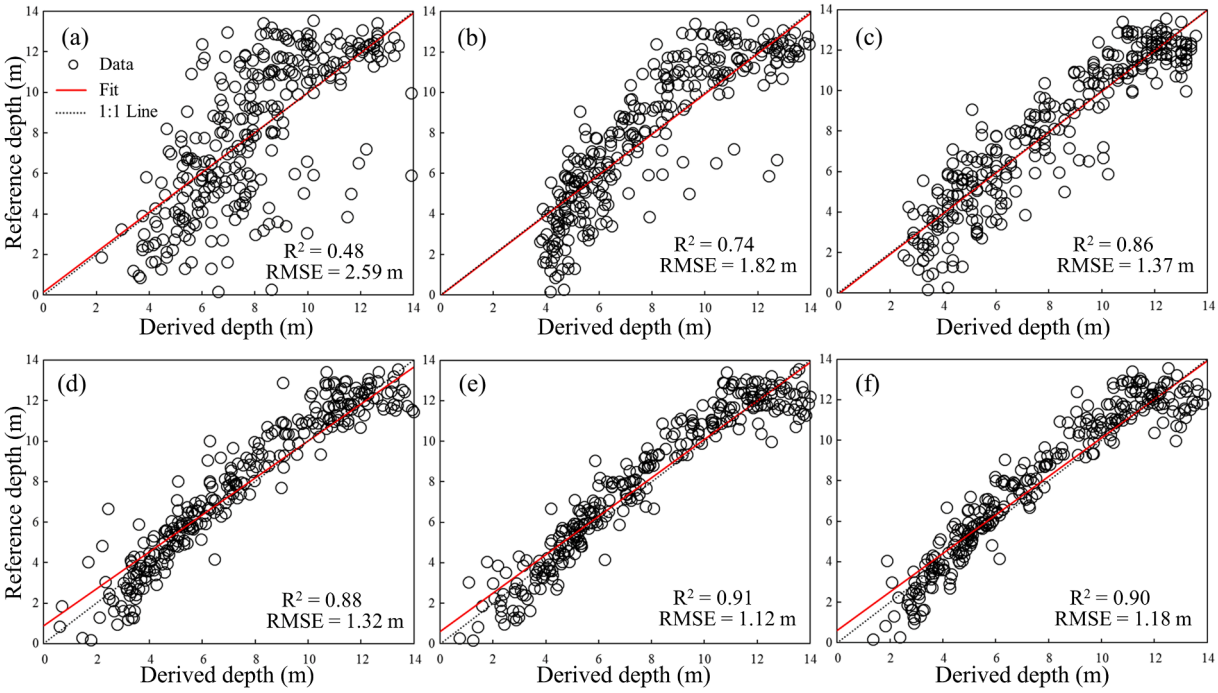

Fig. 8. Accuracy assessment of bathymetric models. Water depth inversion models including (a) ln*Green*, (b) ln*Blue*/ln*Green*, and (c) *Blue-Green*; (d) refraction correction model; combined neural network models including (e) shallow neural network, and (f) deep neural network. (For interpretation of the references to color in this figure legend, the reader is referred to the web version of this article.)

Table 3
Statistics of accuracy assessment metrics for bathymetric models.

Model	R^2	RMSE (m)	MAE (m)	MRE (%)
ln*Green*	0.48	2.59	1.97	60.13
ln*Blue*/ln*Green*	0.74	1.82	1.44	41.47
Blue-Green	0.86	1.37	1.07	32.52
Refraction correction	0.88	1.32	0.98	20.38
Shallow neural network	0.91	1.12	0.89	17.13
Deep neural network	0.90	1.18	0.93	19.84

model had very close MAEs of 1.07 m and 0.98 m, the MRE of the former was much larger than that of the latter.

Among spectral-based bathymetric models, the band difference model *Blue-Green* performed best, because it better reflected the rule of water color changing with water depth of a tufa lake. After refraction correction, the photogrammetric bathymetric model achieved similar overall accuracy to that of the band difference model, and performed better in shallow water due to the involvement of the red band. With strong capability for fitting non-linear problems, neural network-based models accomplished the regression analysis between water color and water depth of the tufa lake with unique spectral features. Moreover, the neural network-based models took advantage of red, green and blue bands simultaneously. Different from the blue and green bands commonly used in the band ratio/difference models, the red band was most sensitive to the depth change in shallow water areas. In addition, the shallow neural network model could satisfy the accuracy requirement of bathymetry with a small number of training samples, but the deep neural network model could not further improve the accuracy without more sample data.

3.3. Improvements from neural network-based methods

The improvements from combined geometric and spectral methods were reflected in the spatial coverage and accuracy of bathymetry. Compared with the depth inversion models and the refraction correction model, the neural network-based combined methods had no obvious invalid bathymetric area and effectively covered the entire water area (Fig. 7). A large number of color-depth training samples for establishing spectral bathymetric models were obtained by refraction-corrected photogrammetric bathymetry, and the local anomalies at the water surface (depressions or bulges) caused by photogrammetric bathymetry were nearly eliminated by spectral-based bathymetric method. As a result, the combined bathymetric methods on neural network models achieved the best bathymetric accuracy without in-situ depth measurements, especially in shallow water depth (Fig. 8).

In addition, the results of combined bathymetry varied according to the adopted neural network architectures. The shallow neural network with single hidden layer satisfied the requirement of combining geometric and spectral methods, and achieved high-accuracy bathymetry (Fig. 8e). Although the deep neural network with more hidden layers did not further improve the bathymetric accuracy, it added more details of water depth distribution in the deep water and tufa mound areas (Fig. 7f).

4. Discussion

4.1. Transferability analysis of bathymetric models

In our study, the trained and validated bathymetric models were also applied to Lying Dragon Lake (Fig. 9a) and Double-Dragon Lake (Fig. 9m) in Shuzheng Valley (Fig. 1). The former is relatively deeper than Spark Lake, and the latter is shallower. According to the official data from Jiuzhai Admin, the maximum depths of Lying Dragon Lake and Double-Dragon Lake is 24 m and 9 m, respectively. Since the pre-earthquake UAV images of the region were captured simultaneously, these two lakes were considered to share the same spectral radiation conditions with Spark Lake. Hence, the transferability of bathymetric models could be evaluated by applying trained and validated models based on Spark Lake to the two adjacent tufa lakes.

As indicated in Fig. 9b-h, the maximum water depths of Lying Dragon Lake derived by bathymetric models were generally low apart

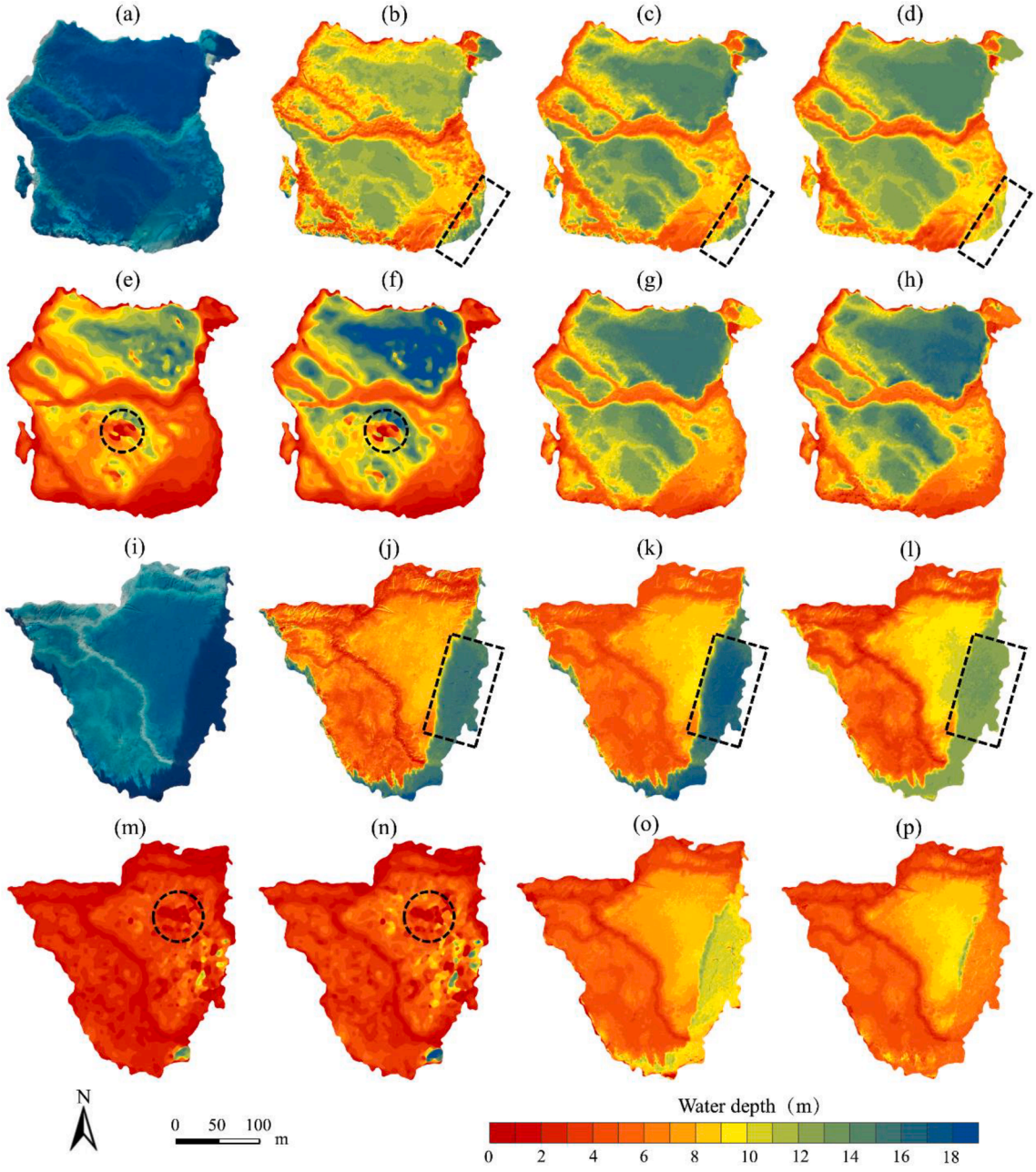

Fig. 9. Transfer applications of bathymetric models. (a) Orthoimage of Lying Dragon Lake; (b)-(h) DBMs derived by ln*Green*, ln*Blue*/ln*Green*, *Blue-Green*, photogrammetry, refraction correction, shallow neural network, and deep neural network. (i) Orthoimage of Double-Dragon Lake; (j)-(p) DBMs derived by ln*Green*, ln*Blue*/ln*Green*, *Blue-Green*, photogrammetry, refraction correction, shallow neural network, and deep neural network. (For interpretation of the references to color in this figure legend, the reader is referred to the web version of this article.)

from that of refraction-correction model. It was possibly caused by the saturation of optical signal in deep water or the refraction effect of light. The depth depressions induced by sparse shadows (dashed rectangles in Fig. 9b-d) and abnormal bulges caused by uniform textures (dashed circles in Fig. 9e, f) were almost removed in the bathymetric maps (Fig. 9g, h) derived by the neural network-based combined methods, especially deep neural network-based one. It indicated that the neural network-based models were transferable to eliminate depth anomalies. As for Double-Dragon Lake, the depth depressions induced by large dark shadows (dashed rectangles in Fig. 9j-l) were remarkable, and abnormal bulges caused by uniform textures (dashed circles in Fig. 9m, n) were still existing. In contrast, the deep neural network-based model was basically able to derive its maximum water depth, even with the interference of the large dark shadow (Fig. 9p). However, a small amount of anomalies were present at the edges of the shadow. The major reason for this phenomenon might be the lack of training samples at the transition zone between shadow and non-shadow areas. The shallow neural network-based model also did worse in the dark shadow areas compared with the deep one. In general, the neural network-based combined models performed well in relatively shallow waters without large dark shadows.

4.2. *Deficiencies and potential remedies*

In this study, the geometric and spectral methods were combined to realize non-contact, high-accuracy and fully-covered bathymetry of clear tufa lakes using neural networks. However, some deficiencies were reflected in the following aspects. First of all, when collecting the

samples from the depth map derived by refraction-corrected photogrammetric bathymetry, the invalid areas with uniform texture were visually identified and manually excluded. The available spectral channels of UAV-acquired visible images were limited for bathymetric modeling compared with hyperspectral imagery (Legleiter and Fosness, 2019; Rossi et al., 2020). There was a lack of quantitative study on the correspondence relationship between the topology of neural network and the number of training samples.

Some measures could be taken to remedy these deficiencies in future applications. For example, the gray level co-occurrence matrix (GLCM) approach (Baraldi and Parmiggiani, 1995) could be used to automatically determine the low texture region in the bathymetric map. With the gradual miniaturization and cost reduction, UAV-borne hyperspectral sensors were expected to be used for bathymetry of tufa lakes. Various topologies of neural networks could be used for combined bathymetry to figure out the optimum correspondence with the number of training samples. In addition, it was beneficial to enhance the effective depth and accuracy of bathymetry if UAV images were captured under conditions of good illumination and small solar altitude angle.

5. Conclusions

In this study, we combined the photogrammetric and spectral-based bathymetric methods to derive DBMs of tufa lakes using UAV images and neural networks. The important conclusions we concluded are as follows:

- The surface elevation and orthoimage produced from UAV-based SfM-MVS photogrammetry could be used as the data sources to derive the DBMs of clear tufa lakes by refraction-corrected photogrammetric bathymetry and spectrally derived bathymetry.
- The refraction-corrected bathymetry tended to cause depth anomalies in the water areas where the lake bed had a uniform texture, while spectral-based bathymetry usually induced abnormal depressions around the tufa mounds with sparse shadows and in the water areas with big shadows.
- The combined bathymetric methods based on neural network models eliminated those depth anomalies occurring in single bathymetric methods and realized fully-covered bathymetry of the tufa lake.
- The neural network model with a single hidden layer achieved the highest accuracy of bathymetry, with the R^2 of 0.91 and the RMSE of 1.12 m (close to 8 % of the maximum depth). The neural network model with multiple hidden layers increased the details of water depth distribution.

Though the combined methods were effective for non-contact, high-accuracy and fully-covered bathymetry of clear tufa lakes, some deficiencies existed including manual exclusion of invalid areas, insufficient spectral channels, undetermined relationship between neural network topology and sample number, and so forth. Therefore, the proposed combined bathymetric methods still have room for improvements. In the future, the studies should involve automatic identification of uniform texture areas based on GLCM, establishment of bathymetric model using hyperspectral images, and determination of the optimum neural network topology according to the number of sample points.

CRediT authorship contribution statement

Jinchen He: Methodology, Software, Validation, Data curation, Visualization, Writing – original draft. **Jiayuan Lin:** Conceptualization, Methodology, Funding acquisition, Supervision, Writing – review & editing. **Xiaohan Liao:** Investigation, Funding acquisition, Project administration.

Declaration of Competing Interest

The authors declare that they have no known competing financial interests or personal relationships that could have appeared to influence the work reported in this paper.

Data availability

Data will be made available on request.

Acknowledgments

This article was jointly supported by the National Natural Science Foundation of China (grant no. 32071678), the Strategic Priority Research Program of the Chinese Academy of Sciences (grant no. XDA19050501), and the Key Research and Development Program of the Sichuan Province (grant no. 2022YFQ0035). The authors would like to thank Yangchun Wang and Xiaolin Du from Institute of Mountain Hazards and Environments, Chinese Academy of Sciences for their help in UAV operations and data acquisition.

References

Alvarez, L., Moreno, H., Segales, A., Pham, T., Pillar-Little, E., Chilson, P., 2018. Merging Unmanned Aerial Systems (UAS) imagery and echo soundings with an adaptive sampling technique for bathymetric surveys. Remote Sens. 10 (9), 1362. https://doi.org/10.3390/rs10091362.

Baraldi, A., Parmiggiani, F., 1995. An investigation of the textural characteristics associated with gray level cooccurrence matrix statistical parameters. IEEE T. Geosci. Remote 33 (2), 293–304. https://doi.org/10.1109/TGRS.1995.8746010.

Chen, Y., Lin, J., Liao, X., 2022. Early detection of tree encroachment in high voltage powerline corridor using growth model and UAV-borne LiDAR. Int. J. Appl. Earth Obs. 108, 102740 https://doi.org/10.1016/j.jag.2022.102740.

Colica, E., D'Amico, S., Iannucci, R., Martino, S., Paciello, A., 2021. Using unmanned aerial vehicle photogrammetry for digital geological surveys: case study of Selmun promontory, northern of Malta. Environ. Earth Sci. 80 (17), 551. https://doi.org/10.1007/s12665-021-09846-6.

Colomina, I., Molina, P., 2014. Unmanned aerial systems for photogrammetry and remote sensing: a review. ISPRS J. Photogramm. Remote Sens. 92, 79–97. https://doi.org/10.1016/j.isprsjprs.2014.02.013.

Currás, A., Zamora, L., Reed, J.M., García-Soto, E., Ferrero, S., Armengol, X., 2012. Climate change and human impact in central Spain during Roman times: High-resolution multi-proxy analysis of a tufa lake record (Somolinos, 1280m asl). Catena 89 (1), 31–53. https://doi.org/10.1016/j.catena.2011.09.009.

Danesh-Yazdi, M., Bayati, M., Tajrishy, M., Chehrenegar, B., 2021. Revisiting bathymetry dynamics in Lake Urmia using extensive field data and high-resolution satellite imagery. J. Hydrol. 603, 126987 https://doi.org/10.1016/j.jhydrol.2021.126987.

David, C.G., Kohl, N., Casella, E., Rovere, A., Ballesteros, P., Schlurmann, T., 2021. Structure-from-Motion on shallow reefs and beaches: potential and limitations of consumer-grade drones to reconstruct topography and bathymetry. Coral Reefs 40 (3), 835–851. https://doi.org/10.1007/s00338-021-02088-9.

Dietrich, J.T., 2017. Bathymetric Structure-from-Motion extracting shallow stream bathymetry from multi-view stereo photogrammetry. Earth Surf. Process. Landf. 42, 355–364. https://doi.org/10.1002/esp.4060.

Eltner, A., Kaiser, A., Castillo, C., Rock, G., Neugirg, F., Abellán, A., 2016. Image-based surface reconstruction in geomorphometry – merits, limits and developments. Earth Surf. Dyn. 4 (2), 359–389. https://doi.org/10.5194/esurf-4-359-2016.

Feng, Y., Huang, Z., Wang, Y., Wan, L., Liu, Y., Zhang, Y., Shan, X., 2021. An SOE-based learning framework using multisource big data for identifying urban functional zones. IEEE J-STARS 14, 7336–7348. https://doi.org/10.1109/JSTARS.2021.3091848.

Fonstad, M.A., Dietrich, J.T., Courville, B.C., Jensen, J.L., Carbonneau, P.E., 2013. Topographic structure from motion: a new development in photogrammetric measurement. Earth Surf. Process. Landf. 38 (4), 421–430. https://doi.org/10.1002/esp.3366.

Granados-Bolaños, S., Quesada-Román, A., Alvarado, G.E., 2021. Low-cost UAV applications in dynamic tropical volcanic landforms. J. Volcanol. Geotherm. Res. 410, 107143 https://doi.org/10.1016/j.jvolgeores.2020.107143.

Guo, Y., Ge, Y., Cui, P., Chen, X., Zhou, L., 2021b. Early and mid-Holocene hydroclimate change recorded in tufa deposits in the Jiuzhaigou gully, eastern Tibetan Plateau. Catena 196, 104834. https://doi.org/10.1016/j.catena.2020.104834.

Guo, H., Yang, H., Qiao, B., Wang, M., Zhu, L., 2021a. Multi-resolution satellite images bathymetry inversion of Bangda Co in the western Tibetan Plateau. Int. J. Remote Sens. 42 (21), 8077–8098. https://doi.org/10.1080/01431161.2021.1970271.

He, J., Lin, J., Ma, M., Liao, X., 2021. Mapping topo-bathymetry of transparent tufa lakes using UAV-based photogrammetry and RGB imagery. Geomorphology 389, 107832. https://doi.org/10.1016/j.geomorph.2021.107832.

Hodúl, M., Bird, S., Knudby, A., Chénier, R., 2018. Satellite derived photogrammetric bathymetry. ISPRS J. Photogramm. Remote Sens. 142, 268–277. https://doi.org/10.1016/j.isprsjprs.2018.06.015.

Iglhaut, J., Cabo, C., Puliti, S., Piermattei, L., O'Connor, J., Rosette, J., 2019. Structure from motion photogrammetry in forestry: a review. Curr. For. Rep. 5 (3), 155–168. https://doi.org/10.1007/s40725-019-00094-3.

James, M.R., Robson, S., 2014. Mitigating systematic error in topographic models derived from UAV and ground-based image networks. Earth Surf. Process. Landf. 39 (10), 1413–1420. https://doi.org/10.1002/esp.3609.

Kim, J.S., Baek, D., Seo, I.W., Shin, J., 2019. Retrieving shallow stream bathymetry from UAV-assisted RGB imagery using a geospatial regression method. Geomorphology 341, 102–114. https://doi.org/10.1016/j.geomorph.2019.05.016.

Legleiter, C., Fosness, R., 2019. Defining the limits of spectrally based bathymetric mapping on a large river. Remote Sens. 11 (6), 665. https://doi.org/10.3390/rs11060665.

Legleiter, C.J., Roberts, D.A., Lawrence, R.L., 2009. Spectrally based remote sensing of river bathymetry. Earth Surf. Process. Landf. 34 (8), 1039–1059. https://doi.org/10.1002/esp.1787.

Lei, H., Wang, X., Hou, H., Su, L., Yu, D., Wang, H., 2017. The earthquake in Jiuzhaigou County of Northern Sichuan, China on August 8, 2017. Nat. Hazards 90 (2), 1021–1030. https://doi.org/10.1007/s11069-017-3064-3.

Li, X., Zhang, M., Xiao, W., Du, J., Sheng, M., Zhu, D., Plenković-Moraj, A., Sun, G., 2020. The color formation mechanism of the blue Karst Lakes in Jiuzhaigou Nature Reserve, Sichuan, China. Water 12 (3), 771. https://doi.org/10.3390/w12030771.

Lin, J., Chen, D., Wu, W., Liao, X., 2022. Estimating aboveground biomass of urban forest trees with dual-source UAV acquired point clouds. Urban For. Urban Gree. 69, 127521 https://doi.org/10.1016/j.ufug.2022.127521.

Liu, L., 2017. Factors affecting tufa degradation in Jiuzhaigou national nature reserve, Sichuan, China. Water 9 (9), 702. https://doi.org/10.3390/w9090702.

Lyzenga, D.R., 1978. Passive remote sensing techniques for mapping water depth and bottom features. Appl. Opt. 17 (3), 379. https://doi.org/10.1364/AO.17.000379.

Maas, H.G., 2015. On the accuracy potential in underwater/multimedia photogrammetry. Sensors-Basel 15 (8), 18140–18152. https://doi.org/10.3390/s150818140.

Mandlburger, G., 2019. Through-water dense image matching for shallow water bathymetry. Photogramm. Eng. Remote Sens. 85, 445–455. https://doi.org/10.14358/PERS.85.6.445.

Mandlburger, G., 2021. Bathymetry from Images, LiDAR, and Sonar. PFG-J. Photogramm. Remote Sens. Geoinf. Sci. 89, 69–70. https://doi.org/10.1007/s41064-021-00153-0.

Mandlburger, G., Kölle, M., Nübel, H., Soergel, U., 2021. BathyNet: a deep neural network for water depth mapping from multispectral aerial images. PFG-J. Photogramm. Remote Sens. Geoinf. Sci. 89, 71–89. https://doi.org/10.1007/s41064-021-00142-3.

Meinen, B.U., Robinson, D.T., 2020. Mapping erosion and deposition in an agricultural landscape: optimization of UAV image acquisition schemes for SfM-MVS. Remote Sens. Environ. 239, 111666 https://doi.org/10.1016/j.rse.2020.111666.

Mulsow, C., Kenner, R., Bühler, Y., Stoffel, A., Maas, H.G., 2018. Subaquatic Digital Elevation Models from Uav-Imagery. ISPRS - International Archives of the Photogrammetry, Remote Sensing and Spatial Information Sciences XLII-2, 739-744. https://doi.org/10.5194/isprs-archives-XLII-2-739-2018.

Niroumand-Jadidi, M., Bovolo, F., Bruzzone, L., 2020. SMART-SDB: Sample-specific multiple band ratio technique for satellite-derived bathymetry. Remote Sens. Environ. 251, 112091 https://doi.org/10.1016/j.rse.2020.112091.

Otero, V., Ruben, V., Satyanarayana, B., Martínez-Espinosa, C., Fisol, M., Ibrahim, M., 2018. Managing mangrove forests from the sky: Forest inventory using field data and Unmanned Aerial Vehicle (UAV) imagery in the Matang Mangrove Forest Reserve, peninsular Malaysia. For. Ecol. Manage. 411, 35–45. https://doi.org/10.1016/j.foreco.2017.12.049.

Qiao, X., Du, J., Lugli, S., Ren, J., Xiao, W., Chen, P., Tang, Y., 2016. Are climate warming and enhanced atmospheric deposition of sulfur and nitrogen threatening tufa landscapes in Jiuzhaigou National Nature Reserve, Sichuan, China? Sci. Total Environ. 562, 724–731. https://doi.org/10.1016/j.scitotenv.2016.04.073.

Rossi, L., Mammi, I., Pelliccia, F., 2020. UAV-derived multispectral bathymetry. Remote Sens. 12 (23), 3897. https://doi.org/10.3390/rs12233897.

Rouse, L.M., Krumnow, J., 2020. On the fly: Strategies for UAV-based archaeological survey in mountainous areas of Central Asia and their implications for landscape research. J. Archaeol. Sci. Rep. 30, 102275 https://doi.org/10.1016/j.jasrep.2020.102275.

Shintani, C., Fonstad, M.A., 2017. Comparing remote-sensing techniques collecting bathymetric data from a gravel-bed river. Int. J. Remote Sens. 38 (8–10), 2883–2902. https://doi.org/10.1080/01431161.2017.1280636.

Slocum, R.K., Parrish, C.E., Simpson, C.H., 2020. Combined geometric-radiometric and neural network approach to shallow bathymetric mapping with UAS imagery. ISPRS J. Photogramm. Remote Sens. 169, 351–363. https://doi.org/10.1016/j.isprsjprs.2020.09.002.

Smith, M.W., Carrivick, J.L., Hooke, J., Kirkby, M.J., 2014. Reconstructing flash flood magnitudes using 'Structure-from-Motion': a rapid assessment tool. J. Hydrol. 519, 1914–1927. https://doi.org/10.1016/j.jhydrol.2014.09.078.

Starek, M.J., Giessel, J., 2017. Fusion of uas-based structure-from-motion and optical inversion for seamless topo-bathymetric mapping. In: 2017 IEEE International Geoscience and Remote Sensing Symposium (IGARSS), pp. 2999–3002. https://doi.org/10.1109/igarss.2017.8127629.

Stumpf, R.P., Holderied, K., Sinclair, M., 2003. Determination of water depth with high-resolution satellite imagery over variable bottom types. Limnol. Oceanogr. 48 (1), 547–556. https://doi.org/10.4319/lo.2003.48.1_part_2.0547.

Vélez-Nicolás, M., García-López, S., Barbero, L., Ruiz-Ortiz, V., Sánchez-Bellón, Á., 2021. Applications of unmanned aerial systems (UASs) in hydrology: a review. Remote Sens. 13 (7), 1359. https://doi.org/10.3390/rs13071359.

Westoby, M.J., Brasington, J., Glasser, N.F., Hambrey, M.J., Reynolds, J.M., 2012. 'Structure-from-Motion' photogrammetry: a low-cost, effective tool for geoscience applications. Geomorphology 179, 300–314. https://doi.org/10.1016/j.geomorph.2012.08.021.

Woodget, A.S., Carbonneau, P.E., Visser, F., Maddock, I.P., 2015. Quantifying submerged fluvial topography using hyperspatial resolution UAS imagery and structure from motion photogrammetry. Earth Surf. Process. Landf. 40 (1), 47–64. https://doi.org/10.1002/esp.3613.

Woodget, A.S., Dietrich, J.T., Wilson, R.T., 2019. Quantifying below-water fluvial geomorphic change: the implications of refraction correction, water surface elevations, and spatially variable error. Remote Sens. 11 (20), 2415. https://doi.org/10.3390/rs11202415.

Xiang, T., Xia, G., Zhang, L., 2019. Mini-unmanned aerial vehicle-based remote sensing: techniques, applications, and prospects. IEEE Geosci. Remote Sens. Mag. 7 (3), 29–63. https://doi.org/10.1109/mgrs.2019.2918840.

Zhou, Y., Lu, L., Li, L., Zhang, Q., Zhang, P., 2021. A generic method to derive coastal bathymetry from satellite photogrammetry for tsunami hazard assessment. e2021GL095142 Geophys. Res. Lett. 48 (21). https://doi.org/10.1029/2021gl095142.